Title

Engineering CoOx-Based Self-Supported Anodes for Pure-Water-Fed Anion-Exchange-Membrane Electrolysis

Authors

Kwak, Minkyoung

Hou, Shujin

Spence, Kieran J

et al.

Publication Date

2025-07-30

DOI

10.26434/chemrxiv-2025-tg6kr

30 July 2025

Engineering CoOx-Based Self-Supported Anodes for Pure-Water-Fed Anion-Exchange-Membrane Electrolysis

Minkyoung Kwak[2,1,3], Shujin Hou[1,3], Kieran J. Spence[4], Tekalign T. Debela[5], Shannon W. Boettcher[1,2,3]

1. University of California, Berkeley
2. University of Oregon
3. Lawrence Berkeley National Laboratory
4. De Nora Tech, LLC
5. Methodist University

Abstract

Commercial membrane electrolyzers rely on acidic fluorocarbon membranes and ionomers, requiring the use of expensive IrOx-based oxygen-evolution catalysts. Anion-exchange-membrane water electrolyzers (AEMWEs) operate in an alkaline environment, enabling the use of non-precious-metal catalysts. Here, we study and engineer CoOx-based catalyst-coated anodes deposited via hydrothermal synthesis directly onto porous transport layers both with and without thermal annealing. Self-supported, nanoneedle-structured Co3O4 anode, formed by annealing the as-synthesized cobalt carbonate hydroxide, Co(CO3)x(OH)y, outperforms the baseline Co3O4 nanoparticle ink-based anode in pure-water-fed AEMWE, due to improved catalyst layer continuity and thus electroactive surface area. The as-synthesized and unannealed Co(CO3)x(OH)y), however, appears to undergo substantial conversion to a more-active CoOx(OH)y phase predominantly at the surface, with nominally Co3+ present and higher electrical conductivity, lowering the cell voltage ~200 mV at 1.0 A#cm-2 in pure-water-fed AEMWE compared to the conventional Co3O4 nanoparticle anodes. We analyze the differences in electrode electrochemical response between pure-water and KOH feed modes finding distinct activation and degradation modes. The Co(CO3)x(OH)y anode shows significant activation and slower degradation linked to the conversion to oxyhydroxide. We propose catalyst layer designs that promote both hydroxide and electron transport, alongside interfacial engineering strategies to obtain high performance while mitigating anode degradation.

 https://doi.org/10.26434/chemrxiv-2025-tg6kr

Keywords

Anion-exchange-membrane water electrolysis, Self-supported catalyst, Catalyst-ionomer interface, Non-precious-group-metal catalyst, Oxygen evolution reaction, CoOx-based anodes, Interface engineering, Durability

Engineering CoO_x-Based Self-Supported Anodes for Pure-Water-Fed Anion-Exchange-Membrane Electrolysis

*Minkyoung Kwak, Shujin Hou, Kieran J. Spence, Tekalign T. Debela, and Shannon W. Boettcher**

M. Kwak, T. T. Debela, S. W. Boettcher
Oregon Center for Electrochemistry, Department of Chemistry and Biochemistry, University of Oregon, Eugene, OR 97403, United States

M. Kwak, S. Hou, S. W. Boettcher
Departments of Chemical & Biomolecular Engineering and Chemistry, University of California, Berkeley, CA 94720, United States
Email: boettcher@berkeley.edu

M. Kwak, S. Hou, S. W. Boettcher
Energy Storage and Distributed Resources Division, Lawrence Berkeley National Laboratory, Berkeley, CA 94720, United States

K. J. Spence
De Nora Tech, LLC, Concord, OH 44077, United States

T. T. Debela
Department of Chemistry and Physical Science, Methodist University, Fayetteville, NC 28311, United States

Keywords: anion-exchange-membrane water electrolysis, self-supported catalyst, catalyst-ionomer interface, non-precious-group-metal catalyst, oxygen evolution reaction

Abstract: Commercial membrane electrolyzers rely on acidic fluorocarbon membranes and ionomers, requiring the use of expensive IrO_x-based oxygen-evolution catalysts. Anion-exchange-membrane water electrolyzers (AEMWEs) operate in an alkaline environment, enabling the use of non-precious-metal catalysts. Here, we study and engineer CoO_x-based catalyst-coated anodes deposited via hydrothermal synthesis directly onto porous transport layers both with and without thermal annealing. Self-supported, nanoneedle-structured Co_3O_4 anode, formed by annealing the as-synthesized cobalt carbonate hydroxide, $Co(CO_3)_x(OH)_y$, outperforms the baseline Co_3O_4 nanoparticle ink-based anode in pure-water-fed AEMWE, due to improved catalyst layer continuity and thus electroactive surface area. The as-synthesized and unannealed $Co(CO_3)_x(OH)_y$), however, appears to undergo substantial conversion to a more-active $CoO_x(OH)_y$ phase predominantly at the surface, with nominally Co^{3+} present and higher electrical conductivity, lowering the cell voltage ~200 mV at 1.0 $A{\cdot}cm^{-2}$ in pure-water-fed AEMWE compared to the conventional Co_3O_4 nanoparticle anodes. We analyze the differences in electrode electrochemical response between pure-water and KOH feed modes finding distinct activation and degradation modes. The $Co(CO_3)_x(OH)_y$ anode shows significant activation and slower degradation linked to the conversion to oxyhydroxide. We propose catalyst layer designs that promote both hydroxide and electron transport, alongside interfacial engineering strategies to obtain high performance while mitigating anode degradation.

1. Introduction

Anion-exchange-membrane water electrolysis (AEMWE) is an emerging technology for H_2 production.[1] In principle, AEMWE combines advantages from proton-exchange-membrane water electrolyzers (PEMWE)—low resistance, zero-gap membrane-electrode assemblies, and dynamic, pure-water operation—and those of liquid alkaline water electrolyzers (AWE) that use of inexpensive materials for catalysts and flow fields. However, AEMWE technology is limited by difficulty in designing high-performance electrodes and their poor durability, in large part from ionomer/membrane instability.[2] Ionomers incorporated in anodes are oxidized during operation, limiting hydroxide transport, and this process is accelerated when the anodes are fed with pure water.[3-5]

In PEMWE, IrO_x-based catalysts have good performance and stability for the oxygen-evolution reaction (OER), and are the only materials used in commercial PEMWE devices.[6-8] IrO_x catalyst nanoparticle inks are prepared with mixtures of ionomer and solvent solutions from which the anode porous-electrode layer is fabricated. This ink-based approach works in part because IrO_x has high electrical conductivity ($\sim 10^4$ $S \cdot cm^{-1}$)[9] so that the electrical resistance of the particle network is sufficiently low despite being mixed with ionomer which reduces particle-particle contacts. Ir is scarce and expensive, though, which limits the scalability of PEM water electrolyzers.[10] AEMWE can use non-precious group metals (non-PGMs) owing to the alkaline environment where many metal oxides are (largely) insoluble.[1,11] Non-PGM anodes in AEMWE devices also outperform Ir-based anodes[4,12] because IrO_2 has moderate OER activity in alkaline conditions.[4,12,13] One issue is that non-PGM catalysts such as those based on Co or Ni oxides are semiconducting and thus have insufficient electrical conductivity to build optimal porous electrodes using ink processing.

Engineering electrode geometry beyond the typical random assemblies of nanoparticles and ionomer from inks can be used to improve electron, ion, and gas transport pathways through the catalyst-ionomer network. Conventionally, catalyst nanoparticles are mixed with ionomers, sometimes with additional binders or conductive non-catalytic supports, in water-alcohol mixed solvents with an optimized catalyst-to-ionomer ratio. These ink solutions are coated by spraying or other means onto porous transport layers (PTLs) or membranes.[3,14] This approach is useful from a manufacturing perspective,[14,15] however, due to structural complexity, controlling or identifying the dominant conduction pathways remains challenging,[16,17] and this complexity

prevents a clear assessment of whether alternative architectures can achieve substantially superior performance.[14] Ionomers partially cover the catalyst particles, increasing interparticle electrical resistance and lowering electric conductivity within the catalyst layer **(Scheme 1**, left).[16-18]. Ionomer and/or binder incorporated in anode catalyst layers can also be oxidized during operation, affecting durability.[4,5,16,17,19]

Self-supported electrodes, where inorganic catalysts are deposited as continuous layers directly on the PTLs, enable engineering the electron-conduction pathways, and the adhesive bonding properties of ionomers between inorganic nanoparticles are unneeded (**Scheme 1**, right). Nano-structuring, in principle, can also be judicially controlled to enhance electroactive surface area, increase catalyst loading, and control surface wetting and bubble removal. These attributes are all useful for robust, high-current-density operation.[16,20] Nanostructure electrode fabrication, however, with such desired properties is nontrivial.

KOH-fed AEMWE cells have been demonstrated with self-supported anodes, mostly using NiFe-oxy(hydroxide)-based OER catalysts.[21-23] The addition of soluble KOH simplifies electrode design dramatically because the liquid electrolyte permeates pores of all sizes in the solid and maximizes catalyst utilization across the entire PTL-supported layer, which is not possible with a solid-ionomer electrolyte using pure-water feed that is ultimately desired for AEMWE.[24] It is further challenging to adopt NiFe-based, and related, self-supported catalysts in pure-water systems because of their poor electrical conductivity when they are not transformed to the more-conductive oxyhydroxide forms due to limited OH^- accessibility,[25] as well as due to durability concerns arising from Fe leaching.[26] Further, the recently developed passivated electrode architecture[27] extends electrode lifetime and integrates naturally with self-supported catalysts due to well-defined catalyst-ionomer interface available to coat prior to ionomer infiltration. This is particularly important as no known ionomers remain stable in the alkaline and oxidizing environment of the AEMWE anode,[5] highlighting the need to understand and advance self-supported electrode designs.

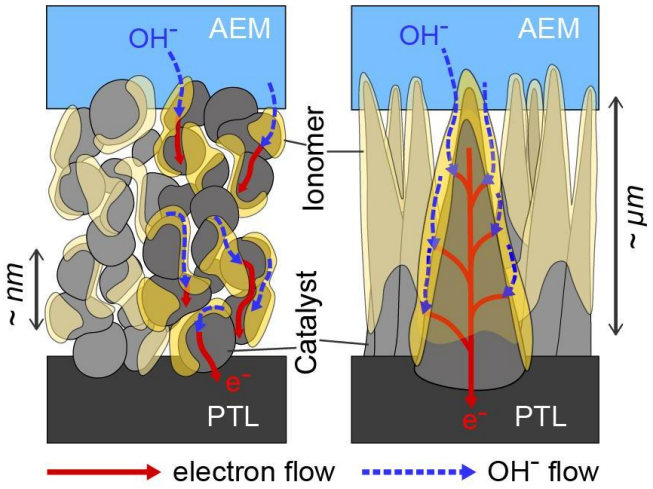

Scheme 1. Comparison of electrode geometry between NP ink-based (left) vs. self-supported (right) anodes. The electronic and ionic pathways are affected by the electrode microstructures forming triple-phase boundaries. The NP ink-based anode possesses regions of disconnected nanoparticles and regions without ionomers covering the surface, while the self-supported anode schematic emphasizes the controllability of micro- and nanoscale electronic and ionic conduction pathways.

Here, Co-based anodes were grown directly on PTLs using a hydrothermal synthesis with controlled materials phase and nanostructure to study the link between electrode response, materials properties, and nanostructure. The resulting PTL-supported $Co(CO_3)_x(OH)_y$ and Co_3O_4 anodes were evaluated in pure-water-fed AEMWE devices and compared to conventional nanoparticle ink-based anodes. By controlling the growth, we show outstanding performance of self-supported $Co(CO_3)_x(OH)_y$ associated with higher electroactive surface areas and improved catalyst layer continuity. The $Co(CO_3)_x(OH)_y$ catalyst layer transformed, partially, into Co^{2+}/Co^{3+} mixed $CoO_x(OH)_y$ phase during the cell activation, providing lower overpotentials at higher current densities compared to the annealed Co_3O_4 anode. Electrode capacitance measurements during the cell activation and continuous operation, however, show that the catalyst-ionomer interfaces degrade under pure-water feed compared to KOH feed. This challenge may be resolved with interfacial engineering strategies building onto self-supported electrodes.

2. Results and Discussion

2.1. Fabrication of Co-based Self-supported Anodes

We deposited nanostructured Co-based OER catalysts on PTLs using a modified hydrothermal synthesis.[28-30] Cobalt nitrate salt and urea were dissolved in DI water, with a Ni-alloy PTL substrate submerged in the solution (Figures S1 and S2). Upon heating up to 100 °C in an oven, urea decomposed and hydrolyzed, releasing carbonate and hydroxide ions[31] that raise the pH and inducing the growth of cobalt carbonate hydroxide (nominally $Co(CO_3)_x(OH)_y$) on the PTL (**Figure 1a**). During the reaction, excess material precipitated at the bottom of the vessel. The $Co(CO_3)_x(OH)_y$ deposited on the PTL can be used as deposited as the OER pre-catalyst or converted to its oxide form via calcination prior to electrochemical testing. The $Co(CO_3)_x(OH)_y$ precipitate was washed with deionized water, centrifuged, and reserved as a powder for characterization.

The morphology and loading of the synthesized $Co(CO_3)_x(OH)_y$ were controlled by modifying hydrothermal reaction times and conditions (see below). Powder X-ray diffraction (PXRD) analysis of the precipitates before and after annealing shows a phase transformation from as-synthesized material, with diffraction features of $Co_6(CO_3)_2(OH)_8 \cdot H_2O$ present, to spinel-phase Co_3O_4 after annealing at 300 °C in air for 2 h (**Figure 1b**). Co 2p X-ray photoelectron spectrum (XPS) shows a shift from predominantly Co^{2+} (in the initial form) to a mixed Co^{2+}/Co^{3+} state (in the oxide form) after annealing, as indicated by changes in the binding energy of the main and satellite peaks and consistent with this phase transformation (**Figure 1c**).[32] The presence of lattice oxygen (530.2 eV) in O 1s XP spectra is also consistent with oxide formation after annealing. Scanning electron microscopy (SEM) images (**Figure 1d**) show a nanoneedle-structured Co_3O_4 on the Ni alloy PTL, synthesized using the optimized hydrothermal synthesis recipe described later. The cross-sectional SEM image obtained after focused-ion-beam (FIB) milling shows that the grown catalyst layer is ~5 μm thick on the PTL.

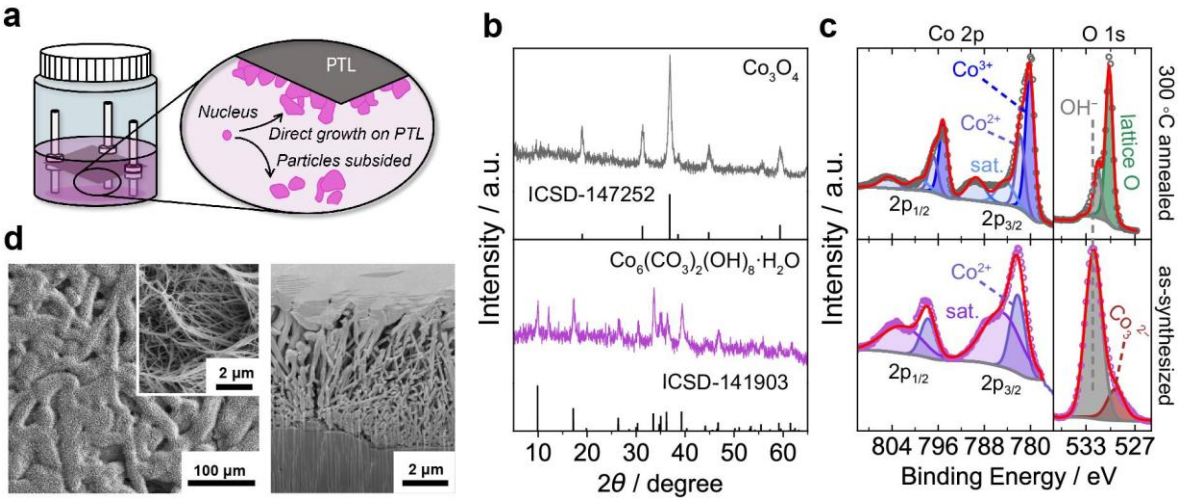

Figure 1. **Electrode materials growth and as-synthesized characterization.** (a) Hydrothermal synthesis schematic. The catalysts were grown directly on the PTL, with some additional solution-phase growth as particles. (b) Powder X-ray diffraction patterns of powders as synthesized and after 300 °C annealing match $Co_6(CO_3)_2(OH)_8 \cdot H_2O$ and Co_3O_4, respectively. (c) XP spectra of catalysts as synthesized and after 300 °C annealing on Ni alloy PTL. After annealing, as-synthesized $Co(CO_3)_x(OH)_y$ transformed to Co_3O_4. (d) SEM top-down and cross-sectional images of prepared Co_3O_4 deposited on Ni alloy PTL showing nanoneedle structure of Co_3O_4 deposited on PTL. A Pt layer was deposited on the top of the sample to facilitate cross-sectioning. SEM images were obtained after annealing to form Co_3O_4 because the non-conductive $Co(CO_3)_x(OH)_y$ samples showed imaging artefacts due to charging in the SEM. No significant morphological differences were observed between the Co_3O_4 and $Co(CO_3)_x(OH)_y$ samples on the length scales observed in the SEM.

2.2. Effect of Electrode Microstructure

To prepare baseline electrodes for comparison, Co_3O_4 catalyst nanoparticles were mixed with PiperION (PAP-TP-85) ionomer in a mixture of isopropyl alcohol (IPA) and deionized water, sonicated, and spray-coated on PTLs to create typical catalyst-ionomer mixed layers.[3] We compared the electrochemical response of this conventional electrode made with a nanoparticle Co_3O_4 loading of 1.7 $mg \cdot cm^{-2}$ with the self-supported annealed Co_3O_4 catalyst layer grown on the Ni alloy PTL with a loading of 1.5 $mg \cdot cm^{-2}$. We incorporate ionomer (PiperION TP-85) onto the self-supported Co_3O_4 anode by dip-coating (with measured ionomer loading of 1.0 ± 0.2 $mg \cdot cm^{-2}$), as well as onto the bare Ni-alloy PTL as a control sample.[27,33] SEM images in Figures S3 and S4 show the incorporated ionomer coats the top of the Co_3O_4 catalyst layer surface. All anodes were

assembled in AEMWE devices with baseline Pt-black cathodes (loading of 2.0 mg·cm^{-2}) and a 40-μm PiperION membrane and tested at 56 ± 1 °C with pure-water feed.

Polarization curves (**Figure 2a**) for AEMWE cells with self-supported Co_3O_4, Co_3O_4 NPs, and bare Ni alloy PTL anodes show that the self-supported Co_3O_4 anode had lower voltages compared to the NP ink-based anode by ~120 mV, and by ~190 mV at 1.0 A·cm^{-2} compared to the bare Ni alloy anode. Electrochemical impedance spectroscopy (EIS) data at 50 mA·cm^{-2} also indicates a lower high frequency resistance (HFR) for the self-supported anode (0.119 Ω·cm^2) compared to the ink-based anode (0.156 Ω·cm^2), and bare Ni alloy anode (0.130 Ω·cm^2). Although the HFR does not fully capture mixed ionic/electronic resistances in the porous electrode due to the parallel equivalent capacitance,[34,35] the lower resistance suggests better electrical interconnection between the catalyst layer and PTL in the self-supported Co_3O_4. The self-supported Co_3O_4 anodes also exhibit higher catalytic activity (**Figure 2b**), with a lower charge-transfer resistance, R_{CT}, (1.08 Ω·cm^2) than the NP-ink based (1.28 Ω·cm^2) and bare Ni alloy (1.27 Ω·cm^2) anodes (the EIS fitting results are in Table S1). This is consistent with lower *iR*-corrected overpotential observed vs. current density (Figure S6) for the self-supported Co_3O_4 anode, indicating that this architecture not only reduces the catalyst-layer resistance but also enhances apparent OER kinetics.

We then measured the (pseudo)capacitive currents from 0.6 to 1.0 V using a two-electrode cell test for different anodes. At 1.0 V, the self-supported anode exhibits approximately four times higher capacitive currents than the ink-based anode (**Figure 2c**). The bare Ni-alloy PTL anode, included as a control, shows minimal capacitive current consistent with small surface area in contact with ionomers. The (pseudo)capacitive voltammogram shapes also differ. The self-supported anode shows substantial capacitive current across the entire voltage window, with a roughly linear capacitance increase as the voltage was scanned positively. In contrast, the nanoparticle anode shows current only on the positive sweep at voltages above 0.6 V, with a less-square charging-box shape at the positive-voltage limit. These observations indicate resistive limitations in accessing the bulk of the porous electrode for nanoparticles, compared to the self-supported catalysts.

The electronic properties of the Co_3O_4 under electrochemical conditions are complex, as Co_3O_4 is a semiconductor with relatively low electronic conductivity.[36] Its surface is redox-active, likely forming cobalt oxyhydroxide and related phases under OER conditions. Cobalt oxyhydroxides are insulators as Co^{2+} but electrically conductive when oxidized to predominantly Co^{3+}.[37] The onset

of substantial capacitive current at 0.6 V likely corresponds to the oxidation of surface Co species, reducing interparticle resistances. The absence of this onset in the self-supported Co_3O_4 electrode, along with the higher (pseudo)capacitive current in the self-supported Co_3O_4, are all consistent with improved electrical conductivity in the ionomer/catalyst porous electrode and a higher electroactive surface area for the self-supported sample.

The interpretation of the AEMWE device metrics and response are consistent with the cross-sectional images in **Figure 2d-e**. In the nanoparticle Co_3O_4 anode, we observed inter-particle disconnections (limiting electron transport) as well as catalyst regions without ionomer coverage (limiting ion transport). In contrast, the self-supported Co_3O_4 show micron-length nanoneedles, with ionomers covering most of the catalyst surface–structures, as represented schematically in **Scheme 1**.

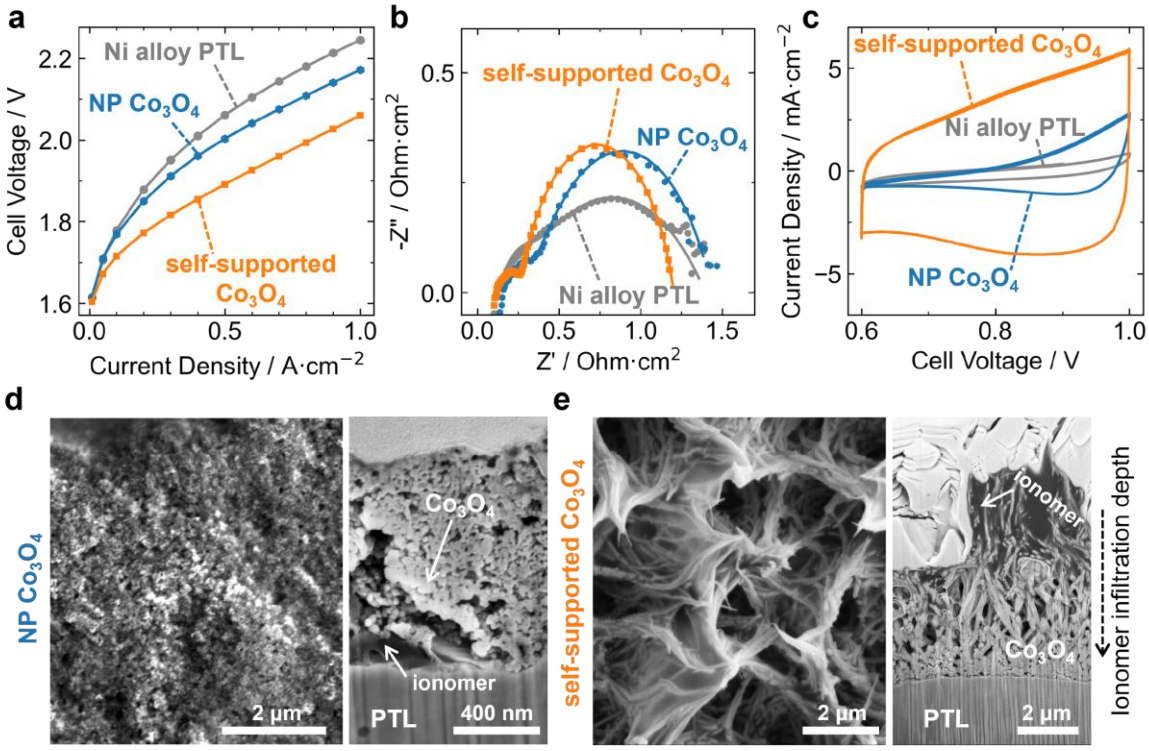

Figure 2. **Electrochemical and microscopy characterization of AEMWE anodes.** (a) Polarization curves of pure-water-fed AEMWE cells at 56 °C with self-supported Co_3O_4 on PTL, NP ink-based Co_3O_4 on PTL, and bare Ni alloy PTL. (b) EIS Nyquist plots at a current density of 50 mA·cm^{-2} and (c) two-electrode cyclic voltammograms at a scan rate of 100 mV·s^{-1} for AEMWE cells with different anodes. Top-view and cross-sectional SEM images of (d) NP Co_3O_4 anode and (e) self-supported Co_3O_4.

The catalyst and ionomer play crucial roles in AEMWE device performance providing pathways for electrons and ions, respectively, in accordance with typical porous-electrode models.[38] If the catalyst loading is too low, the electron and ion transport may remain efficient, but catalytic surface area is insufficient. Excessive catalyst loadings can increase either or both electronic and ionic resistance, negating the benefit of larger catalytic surface area. These effects lead to an optimization tradeoff. As the catalyst electrical conductivity improves, the optimal loading is expected to increase.

Figure 3 shows the impact of catalyst morphology on AEMWE performance for $Co(CO_3)_x(OH)_y$ and Co_3O_4 catalyst layers with various mass loadings. The catalyst loading was controlled by varying hydrothermal reaction times. Longer reactions resulted in thicker $Co(CO_3)_x(OH)_y$ layers deposited on the substrate, which translated to higher Co_3O_4 mass after annealing. The catalyst loading was determined by measuring the mass change of the bare Ni alloy substrate before and after the hydrothermal reaction and 300 °C annealing. The ratio of cobalt nitrate to urea was varied to control $Co(CO_3)_x(OH)_y$ layer growth. Reducing the urea concentration slowed the growth, requiring longer hydrothermal reaction time to reach similar catalyst loadings (**Figure 3a**). Slower growth of $Co(CO_3)_x(OH)_y$ pre-catalyst improved AEMWE device performance (**Figure 3b**, Conditions 2 and 3), likely due to differences in catalyst packing density and nano-structuring.

The ratio of cobalt nitrate to urea also altered catalyst nanostructure (Figure S7). A higher concentration of urea favored nanosheet formation, whereas a lower urea concentration promoted nanoneedle structures with a slower growth rate. During hydrothermal synthesis, cobalt carbonate hydroxide growth is affected by the competition between cobalt-hydroxide and cobalt-carbonate formation, governed by the relative concentrations of hydroxide (local pH) and carbonate ions. It is possible that at lower carbonate concentrations hydroxides are more likely to bind to cobalt ions (such as in **Condition 3**), lowering the local pH and impeding cobalt-carbonate formation.[39] As the reaction proceeds, this may promote anisotropic growth along the z-direction, forming nanoneedles. A recent computational study[40] suggests cobalt carbonate phases maintain structural rigidity, while cobalt hydroxide phases enhance OER activity. One-dimensional (1D) nanoneedles growth reduces the cobalt carbonate phase fraction while increasing $Co(OH)_x$, apparently resulting in a higher active surface area. This is consistent with our results showing that lower urea

concentration reduces carbonate formation, favors 1D growth, and ultimately enhances catalytic performance.

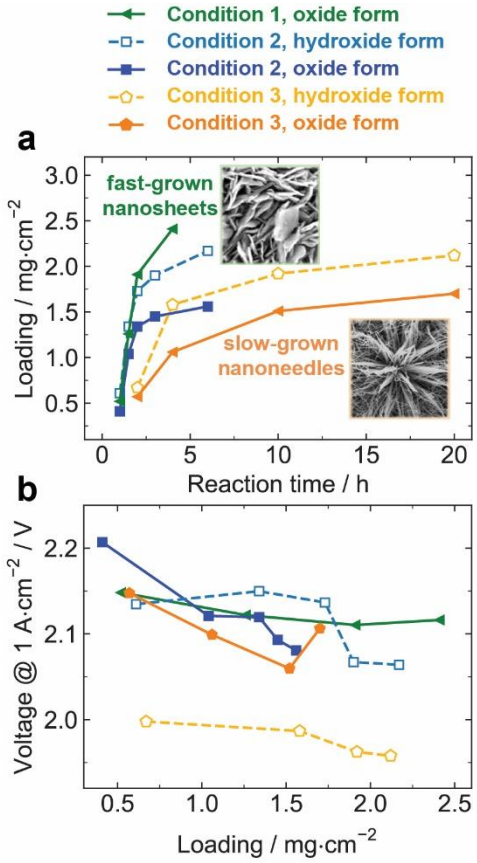

Figure 3. **Reaction conditions and anode performance.** (a) Reaction-time-dependent catalyst loadings with different ratios of cobalt nitrate to urea in hydroxide and oxide forms and (b) corresponding AEMWE cell voltage at 1.0 A·cm^{-2}. **Condition 1:** 27 mmol of cobalt nitrate hexahydrate and 15 mmol of urea used. **Condition 2**: 35 mmol of cobalt nitrate hexahydrate and 15 mmol of urea used. **Condition 3**: 35 mmol of cobalt nitrate hexahydrate and 7.5 mmol urea used. In general, a higher Co precursor to urea ratio leads to slower growth of materials on the substrates and better AEMWE cell performance.

The self-supported Co_3O_4 anode presented in **Figure 2,** along with subsequent data on self-supported $Co(CO_3)_x(OH)_y$ and Co_3O_4 anodes, corresponds to "optimized anodes" prepared using 10 h of hydrothermal synthesis (**Condition 3**). The data in Figure S24 and S25 were obtained during the initial optimization under **Condition 1**, which involved a 4-h hydrothermal synthesis. The impact of ionomer loading on cell performance is discussed below.

2.3. Activation and Degradation of $Co(CO_3)_x(OH)_y$ and Co_3O_4 Anodes

The phase of OER catalysts and their corresponding electrical conductivities affect the AEMWE cell activation and durability because they govern both the catalyst layer resistance[41] and surface reconstruction/activation of Co-based catalyst to the oxyhydroxide form.[42,43] Here, we compared self-supported $Co(CO_3)_x(OH)_y$ and Co_3O_4 coated anodes, each with 1.0 mg·cm^{-2} of PiperION topcoat in an AEMWE device. The self-supported $Co(CO_3)_x(OH)_y$ pre-catalyst exhibits better performance than the self-supported Co_3O_4, with a 90 mV lower cell voltage at 1.0 A·cm^{-2} (**Figure 4a**). The *iR*-corrected overpotential vs. current-density plots (**Figure 4b)** show that while the Tafel slopes of $Co(CO_3)_x(OH)_y$ and Co_3O_4 are similar, $Co(CO_3)_x(OH)_y$ achieves a higher current density at the same overpotential across the entire range. For example, at an overpotential of η = 300 mV, $Co(CO_3)_x(OH)_y$ reaches 6.3 mA·cm^{-2}, whereas that of Co_3O_4 is 2.1 mA·cm^{-2}. At higher current densities > 0.3 A·cm^{-2} (marked as red in the plot), the Co_3O_4 sample shows greater residual overpotentials, likely due to higher ionic and/or electronic resistance within catalyst layer affecting catalyst utilization. Some contribution to the residual overpotential may arise from mass-transport limitation of water or product gas in the porous electrode, although this effect is probably largely misassigned to the residual overpotential in many electrolyzer studies.[41,44] The performance difference highlights the advantages of the as-synthesized $Co(CO_3)_x(OH)_y$ pre-catalyst layer.

To investigate these different performance outcomes between $Co(CO_3)_x(OH)_y$ and Co_3O_4, a freshly assembled AEMWE cell was tested using an alternative procedure instead of the standard break-in process (which involves stepping up the current density to 1.0 A·cm^{-2} in 100 mA·cm^{-2} intervals). Instead, 50 cycles of CV were performed followed by a chronopotentiometry (CP) step holding the current density at 0.5 A·cm^{-2} for 10 min (Figure S8a). These CV-CP steps were repeated 20 times in a loop. The CV measurements examine the evolution of capacitive current, reporting on the electrochemically active surface area. The CP steps activate the catalyst surface under oxidative potential while simultaneously providing information on degradation through the voltage trace required for the step. **Figure 4c** shows the initial CVs up to the third loop. The self-supported $Co(CO_3)_x(OH)_y$ shows a progressive increase of capacitive currents upon each CP step, indicating continuous activation to active surface oxyhydroxide. In contrast, the self-supported Co_3O_4 shows a slight decrease in capacitive currents during the initial three loops. By the 4th loop, the capacitive current of the $Co(CO_3)_x(OH)_y$ pre-catalyst reaches a maximum, whereas for Co_3O_4, it decreases continuously (Figure S8b,c). The voltage responses of $Co(CO_3)_x(OH)_y$ during these

loops stabilize to the steady-state voltages during activation and correlate with the observed increase in capacitance (Figure S8d).

The above analysis shows that $Co(CO_3)_x(OH)_y$ undergoes greater surface reconstruction into the conductive and active $CoO_x(OH)_y$ compared to Co_3O_4. This finding is interesting given that the $Co(CO_3)_x(OH)_y$ exhibits a much lower electrical conductivity than Co_3O_4 in powder form (6.4×10^{-5} mS·cm^{-1} versus 10.6 mS·cm^{-1}, respectively). This difference likely explains why $Co(CO_3)_x(OH)_y$ initially shows small capacitive currents. The as-synthesized $Co(CO_3)_x(OH)_y$ anode was light-purple in color. This anode visibly darkened to black after 1 h of electrolyzer operation, consistent with the proposed structural and electronic transformations. XP spectra reveal the emergence of Co^{2+}/Co^{3+} mixed oxidation states after cell operation (**Figure 4d**).

In all cases, over repeated testing, the CVs show decreasing capacitance while CP steps exhibit an increase in cell voltage, suggesting progressive performance degradation. Consistent with previous studies,[4,5] this degradation is likely driven by ionomer oxidation and catalyst degradation as is discussed further below.

The superior performance of $Co(CO_3)_x(OH)_y$ at high current density may originate from its ability to sustain improved ionic conductivity to the catalyst active sites even when the ionomer is degrading via oxidation. As the $Co(CO_3)_x(OH)_y$ activates, it forms a hydrous oxyhydroxide phase on the surface that hosts water oxidation sites through the three-dimensional, hydrated structure. Like other metal oxides, these hydrated ionomer-free layers likely support a degree of hydroxide ion conductivity, such as found for TiO_2.[45] This effect may provide water-oxidation active sites that are spatially separated from the ionomer and slow performance degradation via interfacial ionomer oxidation. Co_3O_4, however, does not undergo a substantial surface amorphization, leading to active sites for OER in close contact with ionomers that can be degraded under oxidizing potential. This degradation limits OH^- transport to the catalyst surface, particularly at high current and oxidizing potential. For reference, a crystallographic illustration of structural hydroxyl groups in $Co(CO_3)_x(OH)_y$ is shown in Figure S9 for comparison with Co_3O_4.[40,46,47]

Consistent with the above hypothesis, we find the performance gap between $Co(CO_3)_x(OH)_y$ and Co_3O_4 anodes is negligible when the cell was operated with 0.10 M KOH (Figure S10). For these KOH-fed tests, no ionomer topcoats were used to examine the catalyst activation (surface reconstruction) driven purely by OH^- ions supplied from the soluble KOH electrolyte. The continuous OH^- supply also enabled Co_3O_4 to activate more-rapidly yielding similar HFRs, R_{CT},

and kinetic parameters to $Co(CO_3)_x(OH)_y$, even though $Co(OH)_x$ retained higher CV capacitive currents compared to Co_3O_4, suggesting greater electrochemical surface area for the $Co(CO_3)_x(OH)_y$ pre-catalyst anode even under KOH-fed conditions.

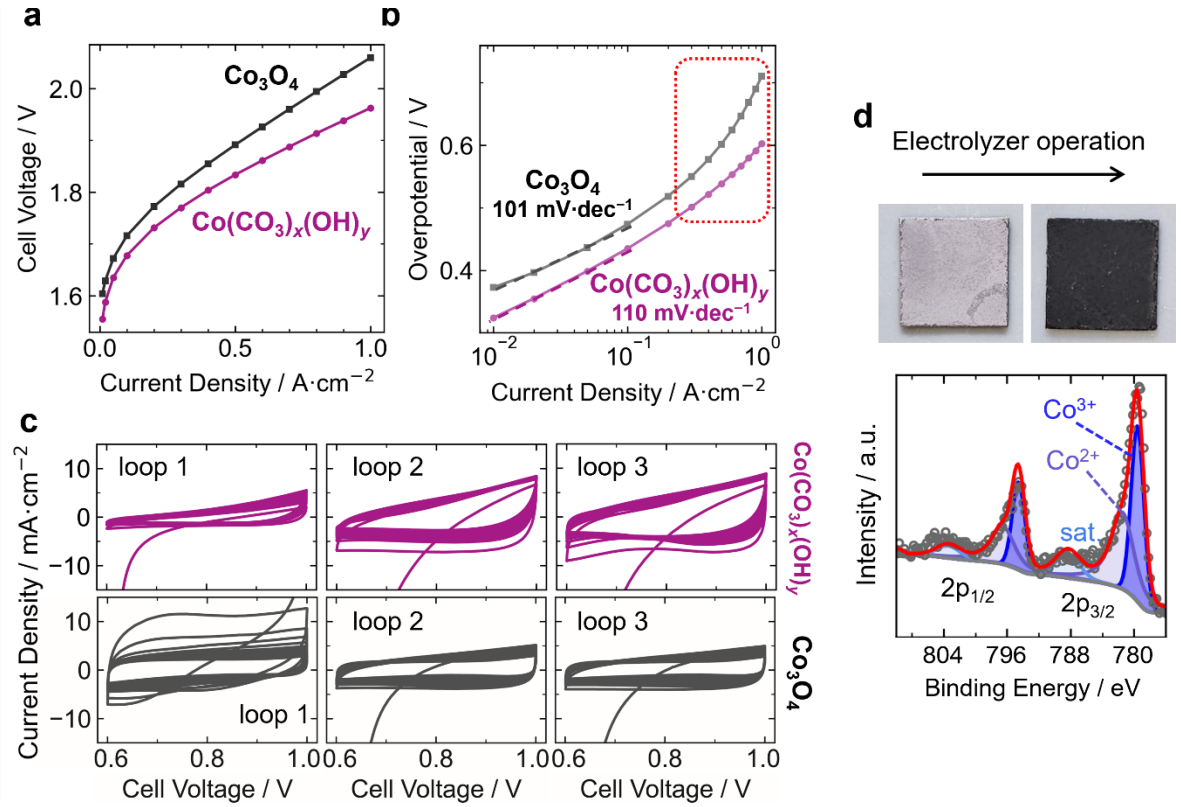

Figure 4. **Time evolution of electrode capacitance and activity.** (a) Polarization curves of pure-water-fed AEMWE cells at 56 °C with self-supported $Co(CO_3)_x(OH)_y$ and Co_3O_4 on Ni-alloy PTLs. (b) *iR*-corrected overpotential versus current density plot of self-supported $Co(CO_3)_x(OH)_y$ and Co_3O_4 on Ni alloy PTLs. (c) CV scans devices made with anodes of $Co(CO_3)_x(OH)_y$ and Co_3O_4 on Ni alloy PTLs in pure-water-fed AEMWE cells. The data shows the initial catalyst activation. (d) Photographs of pristine $Co(CO_3)_x(OH)_y$ anode and one with the anode disassembled after the cell operation (after polarization curve, EIS and CV measurements) and its corresponding Co 2p XP spectrum. The color change of the anode and XP spectra indicate the surface reconstruction to $CoO_x(OH)_y$ after the cell operation.

A durability test at 1.0 $A \cdot cm^{-2}$ was conducted for $Co(CO_3)_x(OH)_y$ and Co_3O_4 anodes in pure-water-fed AEMWE cells, with EIS and CV measurements taken before and after testing (**Figure 6** for $Co(OH)_x(CO_3)_y$ and Figure S11 for Co_3O_4). The Co_3O_4 anode shows faster voltage degradation of ~12 mV/h compared to ~8 mV/h for $Co(CO_3)_x(OH)_y$, primarily driven by an increase in HFR and R_{CT} (Figure S11b). Comparing CVs before and after the durability test,

$Co(CO_3)_x(OH)_y$ retained 84% of its capacitance whereas Co_3O_4 retained 59% (Figure S11d). Post-mortem XPS analysis (Figure S12) reveals that ionomer topcoats were highly oxidized and flushed out after 20 h of cell operation for both anodes. SEM images (Figure S13) also show that most ionomers on the anode surface were gone, and that catalyst layers underneath ionomers were also degraded, which is likely due to higher oxidative potential on the anode as ionomer continuously oxidized. However, the $Co(CO_3)_x(OH)_y$ anode retained its nanoneedle structure, while the Co_3O_4 anode showed significant catalyst layer structural breakdown. The Co_3O_4 anode exhibited a higher voltage during durability testing, suggesting that potential-driven ionomer oxidation may occur more rapidly than on $Co(CO_3)_x(OH)_y$. This accelerated oxidation probably led to local pH drop at the catalyst surface under high OER current (which in the absence of OH^- to consume, generates H^+ from water), promoting the dissolution of Co species, and reducing the structural integrity of Co_3O_4 catalyst layer.

2.4. Effect of Ionomer and Supporting Electrolytes

To systematically assess the impact of ionomer on the electrochemical response and AEMWE performance, we controlled the loading of ionomer topcoats by adjusting the number of dip-coating cycles in a 2 wt% PiperION dispersion. After each dip-coating step, samples were dried at 80 °C, and mass changes were recorded until the target ionomer loading was achieved. A series of self-supported $Co(CO_3)_x(OH)_y$ anodes were prepared with PiperION loadings of 0, 0.1, 0.5, 1.0, and 1.5 $mg \cdot cm^{-2}$, deposited over a 1.9 $mg \cdot cm^{-2}$ of $Co(CO_3)_x(OH)_y$ pre-catalyst layer. Without an ionomer topcoat on the anode, the cell voltage was 2.31 V at 500 $mA \cdot cm^{-2}$ (**Figure 5a**), exhibiting poor kinetics, high cell resistance, and a rapidly increasing voltage from 300 to 500 $mA \cdot cm^{-2}$, indicative of insufficient OH^- supply to the catalyst surface. Adding even 0.1 $mg \cdot cm^{-2}$ of ionomer topcoat improved the cell performance substantially. Increasing the ionomer loading further lowered the cell voltage, but beyond 0.5 $mg \cdot cm^{-2}$ additional loading (up to 1.5 $mg \cdot cm^{-2}$) only resulted in a 20-mV improvement at 1.0 $A \cdot cm^{-2}$.

At 0.1 $mg \cdot cm^{-2}$, the catalyst surface is barely covered with ionomer, while higher ionomer loadings lead to several nanoneedles adhering to each other, networking with ionomer overlayer (Figure S14 and S3). EIS data at 50 $mA \cdot cm^{-2}$ indicates how the HFR and R_{CT} varied with different ionomer topcoat loadings (Figure S15a). The highest HFR and R_{CT} were observed for the sample

without an ionomer topcoat, while those improved with increasing ionomer topcoat loading up to 0.5 mg·cm^{-2}. Beyond this point, no further improvement was observed (Table S2 in SI).

For comparison, *ionomer-free* self-supported $Co(CO_3)_x(OH)_y$ anodes were tested in varying KOH concentrations (**Figure 5b**). Even with 1.0 mM KOH, the performance was notably improved. Increasing KOH concentration lowered the cell voltage to ~1.9 V at 2.0 A·cm^{-2} with 100 mM KOH. Performance improvement of *ionomer-free* anodes with increasing KOH concentrations was also reflected in EIS data (Figure S16a and Table S3), where both HFR and R_{CT} decreased, indicating improved ionic conduction and faster charge-transfer kinetics.

For both ionomer and ionomer-free anodes, we also analyzed the relationship between current densities at a low overpotential (evaluating kinetics) and capacitances (ECSAs). The *iR*-corrected overpotentials as a function of logarithmic current density (Tafel plots) are plotted in Figures S15b,c and S16b. For *ionomer-coated* anodes in pure water, deviations from linear Tafel plots appeared at higher current densities in the Tafel-like plots. In contrast, non-linear responses gradually diminished as the KOH concentration increased in ionomer-free anodes in the KOH system. This difference indicates that the KOH-fed system better maintains OH^- supply, whereas the pure-water system, which relies on the ionomer to provide OH^-, likely experiences an OH^- concentration gradient at the anode surface limiting the OER performance at higher current densities. CVs (Figure S17) show that the capacitive current increases as either ionomer loading or KOH concentration increases, indicating that an adequate local OH^- concentration is central to achieving higher active catalyst surface areas for OER. The capacitances were determined by averaging charges over the sweeping potential range during a CV scan at 100 mV·s^{-1}, which is sufficiently fast to observe limitations of electron and OH^- transport affecting the measured electroactive surface areas.

In general, we find that higher capacitances correlate with higher kinetic current density (at η = 300 mV) as ionomer loading or KOH concentration increases (**Figure 5c**). Although dashed lines are overlayed on the data points to illustrate the trend, it is not intended to represent a specific physical model. Interestingly, at equivalent capacitances between KOH system and pure-water system, the extracted kinetic current density was significantly higher in the KOH system. This could be due to several effects. First, the fast degradation of the ionomer directly at the catalyst surface may be unavoidable in the pure-water system, so the intrinsic activity of the ionomer-contacted OER catalyst might be impossible to measure with ionomer only. Or it may be that the

intrinsic kinetics are in fact different; the cationic charge on the ionomer is all attached to the backbone of the polymer which prevents substantial conformational flexibility. The cations themselves are much larger than K^+. Both these effects might modulate the intrinsic site-specific reaction rates for the OER and merits further study.

The activation behavior of *ionomer-free* and *ionomer-coated* $Co(CO_3)_x(OH)_y$ anodes was compared in AEMWE cells with dilute (0.1 mM) and more-concentrated (100 mM) KOH feeds. With 0.1 mM KOH, the *ionomer-free* anode requires a large overpotential to activate and stabilize, resulting in a significant cell-voltage gap compared to *ionomer-coated* anode during the break-in procedure, where the current density gradually steps up (Figure S18). In 100 mM KOH, this performance gap is small (Figure S19d), and EIS data even indicates that the ionomer topcoat introduced additional resistance, shown by the lower HFR observed in the absence of ionomer (Figure S19e). While the capacitance increased with the presence of the ionomer topcoat with pure water and dilute KOH feed, it decreased when ionomer was incorporated in the cell with 100 mM KOH feed (Figures S17a and S19c,f). This suggests that at higher KOH concentration, the ionomer topcoat may hinder OH^- accessibility at the catalyst surface.

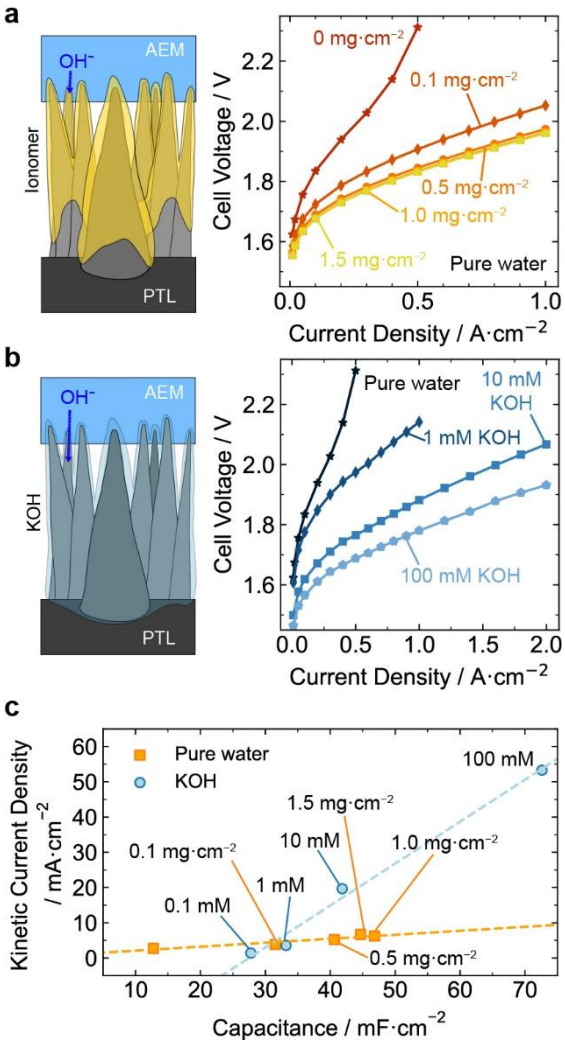

Figure. 5. Comparing anodes in with ionomer and in KOH electrolyte. (a) Scheme of *ionomer-coated* $Co(CO_3)_x(OH)_y$ anode and its polarization curves of pure-water-fed AEMWE cells at 56 °C with different PiperION ionomer topcoat loadings. (b) Scheme of *ionomer-free* $Co(CO_3)_x(OH)_y$ anode and its polarization curves of AEMWE cells at 56 °C with different concentrations of KOH feed. (c) Plot of kinetic current densities at an overpotential of 300 mV as a function of capacitance for *ionomer-coated* anodes in pure water and *ionomer-free* anodes in KOH.

With an understanding of $Co(CO_3)_x(OH)_y$ pre-catalyst activation and the effects of ionomer and KOH supporting electrolyte on the cell performance, durability tests were then conducted for 1.0 $mg \cdot cm^{-2}$ ionomer-coated $Co(CO_3)_x(OH)_y$ anodes in three different systems: pure-water feed, 100 mM KOH feed, and a cell activated with 100 mM KOH then switched to pure-water feed. All cells were operated at 1.0 $A \cdot cm^{-2}$ for 20 h, with EIS and CV measurements recorded at the beginning of life (BOL) and end of life (EOL). For the KOH-to-pure-water system, the cell was initially operated with 100 mM KOH feed for 2 h, and EIS and CV collected to monitor the initial catalyst

activation (**Int I**). Subsequently, the cell was flushed with > 4 L of pure water to remove the KOH (with the exception perhaps of strongly absorbed species) then the operation was continued for an additional hour with the cell connected and recirculated with a large water reservoir (~15 L). After these steps, the durability test was interrupted to obtain another set of EIS and CV (**Int II**) to assess how the activated catalyst changed upon transitioning to the pure-water system. In the pure-water system, the cell voltage increased at 8.0 $mV \cdot h^{-1}$ over the final 10 h of the operation (**Figure 6a**). In contrast, when KOH was fed to the cell, cell voltage improved by ~150 mV, and the degradation rate dropped significantly to 0.24 $mV \cdot h^{-1}$. Upon flushing KOH out with pure water, the cell voltage initially increased by ~100 mV. With continuous operation under pure-water feed, the cell voltage degraded at a rate of 2.7 $mV \cdot h^{-1}$.

CVs obtained at different stages of operation across the three different feed systems are compared in **Figure 6b**. In the KOH-fed cell, capacitance remained largely unchanged between the BOL and EOL, suggesting that $Co(CO_3)_x(OH)_y$ with the reconstructed $CoO_x(OH)_y$ surface layer maintained high catalyst utilization with sufficient OH^- flux. Supporting electrolyte suppresses ionomer oxidation, stabilizing the catalyst-ionomer interface, possibly by screening charge interactions at the catalyst-ionomer interface or preventing absorption.[5,48]

When the KOH-fed cell was switched to pure-water operation, the CV at the **Int II** stage showed pseudocapacitive behavior with distinct redox features around 0.9 to 1.0 V that are only marginally enhanced relative to the pure-water BOL sample suggesting the largely effective removal of KOH from the catalyst surface, along with possible charge screening effects. Continued cell operation beyond 10 h did not significantly change the CV features in the KOH-to-pure-water system (compare **Int II** vs. EOL), reflecting a moderate voltage degradation rate in this transition system. The capacitances at different stages are summarized in Figure S20. In contrast, the pure-water-fed system exhibited a lower initial capacitance (BOL), which decreased significantly by EOL, indicating that catalyst was not fully activated in pure water, leading to a higher cell voltage as well as a faster voltage degradation rate. It is possible that the higher cell voltage from less-activated catalysts (pure-water only) led to accelerated ionomer oxidation, hence reducing the active surface area.

EIS data in **Figure 6c** is consistent with the above cell polarization and voltammetry data, showing similar EIS plots at the BOL and EOL for KOH system, reflecting stable cell voltage throughout the operation. In contrast, the kinetics (i.e. R_{CT}) changed significantly from BOL to

EOL in the pure-water system, consistent with the fast voltage increase and degradation. When the cell operated in KOH was flushed with pure water, the initial EIS plots remained similar with slight improvement then degradation in R_{CT} (BOL→**Int I**→**Int II**); however, extended operation in pure water led to degraded kinetics at EOL. This suggests that although the catalyst was fully activated in KOH without apparently substantial ionomer degradation the limited OH^- accessibility in the pure-water system initiated ionomer degradation at the catalyst surface. This degradation likely contributed to a gradual decrease in capacity as well as an increase in R_{CT}. The increase in R_{CT} was less severe compared to the EOL analysis of the device tested in pure water only (Table S4).

In the pure-water system, anodes suffered severe structural damage following operation, as evidenced by ionomer oxidation and catalyst degradation (Figures S12 and S13). In the KOH and KOH-to-pure-water systems, the catalyst-ionomer interface remained more stable. The SEM images in Figure S21 show that ionomer coverage was retained in both systems and XPS data indicates a substantial reduction in ionomer oxidation (Figure S22). This stability is likely due to catalyst surface-charge-screening effect from supporting electrolytes and lower oxidation potentials, suggesting a small degree of interfacial stabilization from the pre-treatment in KOH that may leave residual absorbed cations.

In **Figure 6d**, we present hypothesized molecular-level models of the anode catalyst-ionomer interfacial structures in different feed modes. In the pure-water system, Co-based anode catalysts with hydroxyl groups, partially deprotonated in the alkaline conditions (pH > PZC ≈ 9),[49] can interact with the ionomer backbones or cationic groups and may also specifically absorb. When the oxidative potential is applied to the anode, $Co(OH)_x$ forms $CoO_x(OH)_y$ from oxidation of the metal centers at the catalyst surface. The direct contact between the active $CoO_x(OH)_y$ and ionomer promotes electrochemical oxidation of ionomer, a dominant failure mechanism. However, when the cell is flooded with KOH, K^+ may adsorb at the catalyst surface, reducing absorption either via molecular or electrostatic mechanisms.[5,48]

At a given oxidative potential, the catalyst surface reconstructs to a more-active phase in both pure-water and KOH-fed systems. The degree of catalyst reconstruction appears limited to available OH^- from ionomer contacting the catalyst in the pure-water system, while mobile KOH increases the formation of $CoO_x(OH)_y$. From this picture, we hypothesize that the improved performance and durability of the KOH-to-pure-water compared to pure-water-only cell is due to KOH-modulated activation of $Co(CO_3)_x(OH)_y$. Even after flushing KOH out with pure water,

residual K^+ ions may interact with reconstructed catalyst surface, slowing ionomer oxidation and lowering the cell voltage.

The above data and analysis suggest that pre-absorption or activation in other electrolytes might be useful in exploring how to stabilize the interface. Based on, for example, hard/soft acid-base ideas,[50,51] other ions with stronger interactions with the metal oxy(hydroxide) catalyst surface may provide additional pathways to prevent direct interaction between the catalyst and ionomer and suppress ionomer oxidation. The nature of catalyst-counterion interactions in the supporting electrolyte probably depends on both catalyst surface charge and the ionic charge, and radius of cations.

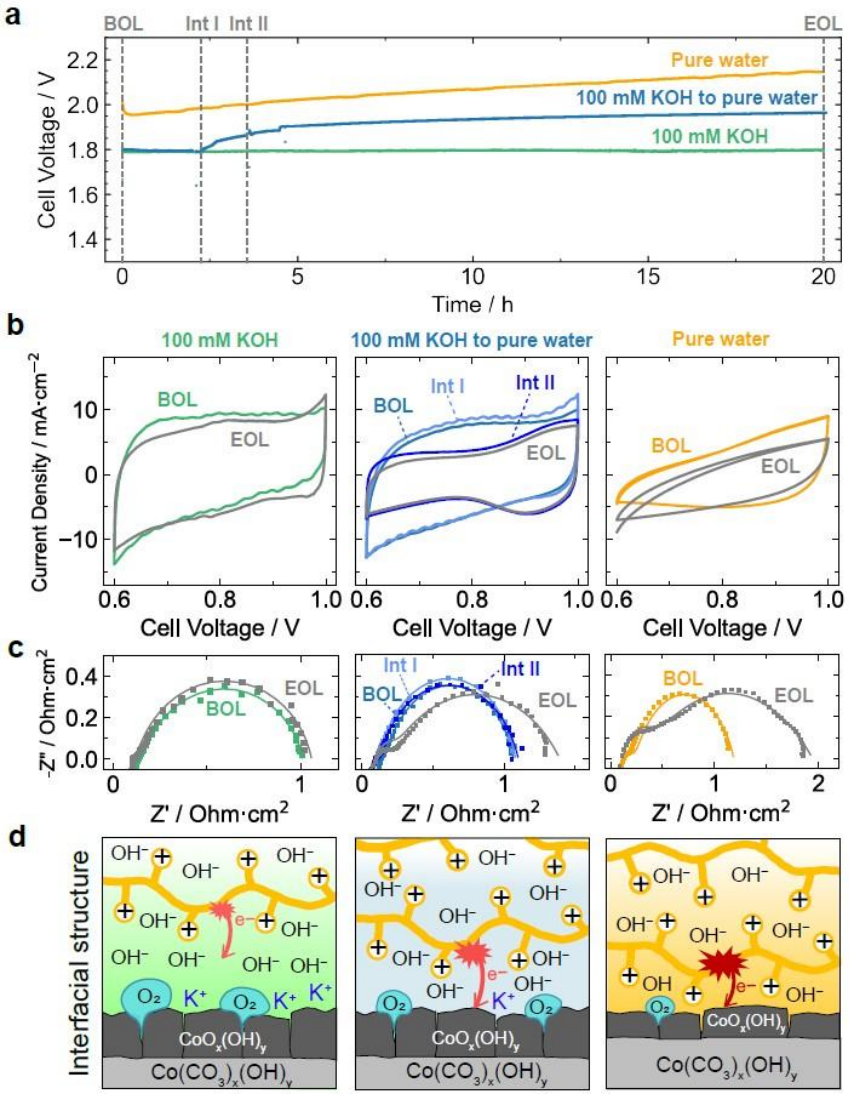

Figure 6. **Understanding degradation modes for AEMWE anodes water and KOH feed.** (a) Durability test of KOH-fed, KOH-to-pure-water-fed, and pure-water-fed AEMWE cells with PiperION coated $Co(CO_3)_x(OH)_y$ anodes. The cell was held at 1.0 A·cm^{-2} at 56 °C. During the durability test, CV and EIS were obtained at different stages. For the KOH-to-pure-water-fed system, the cell was activated in KOH for 2 h (until **Int I**) then flushed with pure water (until **Int II**). Corresponding (b) CVs at a scan rate of 100 mV·s^{-1}, and (c) EIS curves at a current density of 50 mA·cm^{-2}. (d) Molecular-level schemes of catalyst-ionomer interfaces with different feed modes at the end of life. Related processes include (*i*) the catalyst surface interacting with KOH supporting electrolyte and/or ionomer; (*ii*) surface reconstruction of $Co(CO_3)_x(OH)_y$ to more active and conductive $CoO_x(OH)_y$ at oxidative potentials (*iii*) oxygen evolution reaction; and (*iv*) oxidation. The degree of catalyst surface reconstruction is higher with KOH feed due to mobile K^+ and OH^-. Less ionomer degradation is evident with electrolyte screening surface charge of the catalyst and physical moving ionomer further away from the catalyst surface. In the pure-water system, direct contact

between active catalyst and ionomer leads to severe ionomer oxidation. In the KOH-to-pure-water system, activated $CoO_x(OH)_y$ and residual K^+ extended lifetime of the cell compared to the pure-water system.

The durability of self-supported anodes in pure-water AEMWE is limited (**Figure 6a**) due to ionomer oxidation and likely subsequent local acidification under OER (which consumes OH^-). This can trigger catalyst degradation by dissolution of catalysts in addition to mechanical breakdown. In the self-supported anode geometry, where most of the catalyst surface is covered with ionomer, facile electron transport through the catalyst layer may both lower voltage but also facilitate the ionomer degradation, in turn accelerating cell degradation. For the NP-based anode, the disconnection between catalyst nanoparticles, caused by electronically insulating ionomers covering the catalyst surface results in a lower active surface area, and inferior performance, but somewhat lower voltage degradation rate (Figure S23).

To study and mitigate the degradation of these self-supported anodes, we applied a passivation layer based on our previous study.[27] A 3.5-nm thick HfO_x coating, deposited by atomic-layer deposition, was introduced to stabilize the catalyst-ionomer interface. While the HfO_x passivation layer led to an increase in the cell voltage by ~200 mV at 1.0 $A \cdot cm^{-2}$ (Figure S24a), it also restricted hydroxide transport to the Co_3O_4 catalyst, resulting in a lower (pseudo)capacitive current compared to the uncoated Co_3O_4 anode (Figure S24b). During a durability test at 500 $mA \cdot cm^{-2}$, HfO_x coated Co_3O_4 exhibited a continuous improvement with a cell voltage change rate of −3.8 $mV \cdot h^{-1}$ (Figure S24c), superior to the uncoated Co_3O_4 that degraded at 18 $mV \cdot h^{-1}$. Without the HfO_x coating, both HFR and total charge transfer resistance increased substantially after 15 h of the durability test (Figures S24d), while with the HfO_x coating, the total charge-transfer resistance decreased after the durability run.

The SEM images in Figures S25 show that HfO_x coated anode successfully maintained the ionomer topcoat after the durability test, while uncoated anode showed severe ionomer-catalyst surface damage. This is consistent with previous studies on ionomer oxidation in pure-water systems[4,5,27] and supports the hypothesis that interface engineering can suppress ionomer degradation. While this 15-h test is not sufficient to demonstrate the long-term viability of self-supported anodes with passivation coatings for commercial applications, it motivates further studies to optimize passivation coatings parameters, particularly controlling porosity and ion

transport through the layers, and conducting extended test under harsher conditions, such as higher temperatures and current densities, to fully evaluate the practical stability of enhanced designs.

3. Conclusion

Self-supported, non-PGM Co-based anodes for AEMWE were prepared *via* a simple hydrothermal reaction. The self-supported Co_3O_4 anode was compared to the conventional Co_3O_4 nanoparticle ink-based anode, illustrating the importance of catalyst connectivity in device electrochemical response. We compared self-supported $Co(CO_3)_x(OH)_y$ and Co_3O_4 anodes and discovered improved performance and durability for $Co(CO_3)_x(OH)_y$ which readily converted to a more-active and water-permeated $CoO_x(OH)_y$ phase. Self-supported anodes in a pure-water-fed AEMWE with ionomer solid electrolyte had less interfacial capacitance and active surface area than equivalent anodes with KOH supporting electrolytes. These data lead to a molecular picture whereby the systems with the best performance had a water-permeated $CoO_x(OH)_y$ phase present that is able to conduct both electrons and hydroxide. These phases have improved durability when modified with even small amounts of KOH in addition to the solid ionomer which help screen interfacial ionomer absorption and ionomer oxidation. A dedicated study of interface structure, however, is needed to fully test this hypothesis.

With these new insights into the anode catalyst structures and their interfaces with ionomer and electrolyte, we suggest methods to engineer improved self-supported anodes for pure-water-fed AEMWE systems. First, the current ionomer coating process is simple, either spray coating or dip coating to meet the desired ionomer topcoat loading. These non-optimized methods result in the ionomer coating the surface of the catalyst layer and some of the pores of the PTL. To maximize the catalyst-ionomer interface area, better methods to infiltrate ionomer through the deep pores of the catalyst coating are needed that co-optimize interface properties, ion transport, and reactant and product transport. The local pH and hydroxide-ion conductivity near the catalyst surface might also be improved with ionomers with higher ion exchange capacities (IECs),[33] for example specifically in the interface layer. The catalyst layer itself can be improved by targeting OER catalysts that have metallic conductivity, such as perovskite oxides,[52] and that can be engineered with appropriate three-dimensional structures and with controlled reconstruction of surface structures, but such metallic catalysts will likely need specific interface passivation layer development to prevent ionomer oxidation. Pre-activation or *in-situ* activation of such synthesized

samples might be controlled and optimized for performance and durability by controlling the extent of oxyhydroxide formation. These more-active, electrically conductive, and morphology-engineered catalysts could then be modified with surface passivation layers, better designed to promote catalysis and hydroxide ion transport, building on the preliminary examples with the HfO_x coating demonstrated here.

Experimental Methods

Hydrothermal growth of $Co(CO_3)_x(OH)_y$ and Co_3O_4 on Ni alloy PTL: In a glass jar, 35 mmol of $Co(NO_3)_2$ hexahydrate and 7.5 mmol of urea, $CO(NH_2)_2$, were dissolved in 30 mL of 18.2 MΩ·cm high-purity water. A Ni alloy PTL substrate (Hastelloy X, Technetics Inc.) was cut in 3.3 × 3.3 cm^2, backside-masked with a 0.002-inch-thick polytetrafluoroethylene (PTFE) film and supported by PTFE threaded rods and Nylon nuts. When the tripod-supported substrate was submerged in the solution and heated up to 100 °C in an oven, $Co(CO_3)_x(OH)_y$ grew on the PTL as well as precipitated. The hydrothermal reaction time was varied to control the loading of deposited material with 10 h found to be optimum. After hydrothermal synthesis, the sample was taken out of the jar, washed with excess pure water, and dried overnight to measure the mass loading. $Co(NO_3)_2$ hexahydrate to urea ratio was optimized as the recipe shown here. To prepare Co_3O_4 anode, the as-synthesized $Co(CO_3)_x(OH)_y$ sample was annealed at 300 °C for 2 h.

Preparation of HfO_x coating: A HfO_x coating was deposited on top of a self-supported Co_3O_4 anode using an atomic layer deposition system (Savannah, Ultratech). A HfO_x layer 3.5 nm thick was deposited from repetitive cycles of ALD deposition with 0.4 s pulses of water and 0.015 s pulses of tetrakis(dimethylamido)hafnium(IV), TDMAHf, with an interval of 5 s between each pulse at 250 °C. A Si wafer was put inside the ALD chamber along with Co_3O_4 coated Ni alloy PTL to measure the thickness of the HfO_x film using an ellipsometer.

Materials Characterization: Powder X-ray diffraction (PXRD) patterns were obtained to identify the dominant crystalline phase(s) of the prepared catalyst with a Bruker D2 Phaser benchtop diffractometer (Cu K-alpha radiation, λ=1.54 Å). Powder electrical conductivity was measured following literature procedures.[4] For example, 100 mg of catalyst powder was pressed to form a pellet, and a current-voltage curve was obtained and used to estimate the electrical conductivity of the pellet. A M-2000 spectroscopic ellipsometer (J.A. Woollam) was used to calculate HfO_x ALD

film on a Si wafer. The optical response from 240–1688 nm was fitted with a model of a dielectric film on a Si substrate. Scanning electron microscopy (SEM) images were obtained with a Helios Hydra (Thermo Fisher), to understand the nanostructure of catalyst layers. SEM characterization was performed at 5 kV using ETD or TLD mode. The anodes were cross-sectioned using a plasma focused-ion-beam (PFIB) and SEM images were obtained with elemental maps using an EDS analyzer. X-ray photoelectron spectroscopy (XPS) measurements were conducted using an ESCALAB 250 (Thermo Scientific) using an Al Kα mono-chromated source with 20 eV pass energy (500 µm spot-size). The binding energies were calibrated with the C 1s spectra (main carbon peaks at 284.8 eV). For post-mortem XPS analysis, cell operated anodes were soaked in 3 M NaCl to ion-exchange ionomer from OH^- to Cl^- form, washed with pure water vigorously and dried in air before XPS measurements.

Electrode preparation: NP-based electrodes were prepared by spray-coating ink solutions to anode and cathode PTLs. The catalyst ink solution was prepared by mixing 100 mg of nanocatalyst powder, 200 mg of 5 wt% PiperION dispersion (TP-85, Versogen), 0.5 g of 18.2 MΩ·cm high-purity water, and 1.7 g of isopropyl alcohol. The mixed solution was sonicated for 2 h with a cooling water line immersed in the sonication bath. Pt black (Fuel Cell Store) ink solution was spray-coated on carbon paper (Toray 090, Fuel Cell Store) to prepare cathodes. Co_3O_4 (30–50 nm, US Research Nanomaterials) ink solution was spray-coated on Ni-alloy PTL as anodes. During spray-coating, the substrates were fixed on a hot plate at 80 °C to dry out solvent and form catalyst layer. After 1.5–2 $mg \cdot cm^{-2}$ of catalyst layer loading was obtained, a thin ionomer topcoat was applied by spraying 2 wt% PiperION dispersion. For self-supported anodes after hydrothermal synthesis, PiperION topcoats were applied by dipping the anode into 2 wt% PiperION dispersion with the catalyst-coated sides facing down. After dipping, the samples were placed on the hot plate at 80 °C to remove solvent. The dipping-and-drying step was repeated until the target ionomer loading was obtained. The loading of ionomer topcoat was calculated from the mass difference of anodes before and after dip-coating. Ionomer-free anodes were tested in the electrolyzer without this dip-coating procedure.

Membrane electrode assembly (MEA) fabrication: The AEMWE single cell assembly was adopted from literature.[3,27] A preconditioned AEM (40 µm PiperION, Versogen) was sandwiched between 1.0 cm^2 precut cathode and anode electrodes with gaskets. The MEA was compressed in

flow fields and bipolar plates. 18.2 MΩ·cm high-purity water was supplied to both anode and cathode from a water tank at 60 $mL \cdot m^{-1}$. The cell temperature was set to 56 ± 1 °C with the water tank (15 L) at 62 °C. Different concentrations of KOH were fed to both anode and cathode for KOH concentration-dependent performance measurements. For a KOH-to-pure-water cell operation, the cell was initially fed with 100 mM KOH, then flushed with pure water (> 4 L) to remove any residual KOH. Lastly, pure water was recirculated in the cell from the water tank.

AEMWE single cell operation: The electrolyzer test was conducted with a BioLogic VSP-300 potentiostat equipped with a 10 A/5 V booster. Starting from 100 $mA \cdot cm^{-2}$, the current applied to the cell was stepped up to 1.0 $A \cdot cm^{-2}$ with an interval of 100 $mA \cdot cm^{-2}$ as a cell break-in procedure. The current was held for 2 min for each current step. After breaking in the cell, the current was stepped down with an interval of 100 $mA \cdot cm^{-2}$, held for 10 s for each step, back to 100 $mA \cdot cm^{-2}$ with two additional current steps to 50 and 10 $mA \cdot cm^{-2}$ to obtain a polarization curve. Electrochemical impedance was measured at 50 $mA \cdot cm^{-2}$ with a frequency range of 1 MHz to 100 mHz. Cyclic voltammograms were obtained by sweeping a cell voltage between 0.6 V and 1 V with a scan rate of 100 $mV \cdot s^{-1}$. For durability tests, the cell was held at either 500 $mA \cdot cm^{-2}$ or 1 $A \cdot cm^{-2}$ for a certain period. EIS and CV measurements were repeated after the durability test. When the cell was operated with KOH feed, the current was held up to 2.0 $A \cdot cm^{-2}$ for the initial cell break-in and obtaining polarization curve. To monitor the activation and degradation of $Co(OH)_x(CO_3)_y$ and Co_3O_4 anodes, the cell was cycled with a voltage range of 0.6 V to 1.0 V 50 times (CVs) then a constant current of 0.5 $A \cdot cm^{-2}$ was applied for 10 min (CP). The CV and CP steps were repeated 20 times in a loop.

Supporting Information

Supporting Information is available from the Wiley Online Library or from the author.

Acknowledgements

The catalyst science and development work were supported by the National Science Foundation, Chemical Catalysis Program award #2400195. The electrolyzer device work was supported by the U.S. Department of Energy's Office of Energy Efficiency and Renewable Energy (EERE) under the Hydrogen and Fuel Cell Technologies Office (HFTO) under award DE-EE0011322 and by De

Nora Tech, LLC. We acknowledge the use of shared instrumentation in the Center for Advanced Materials Characterization in Oregon (CAMCOR). M.K. thanks Dr. Paul Kempler and Dr. Arunavo Chakraborty for insightful discussions.

Conflict of Interest

K.J.S. is an employee of De Nora Tech, which produces commercial electrodes for water electrolyzers.

Author contributions

M.K. and S.W.B. conceptualized and led the project. M.K. prepared samples, collected electrolyzer data, and characterized samples. S.H. and K.J.S. provided feedback on the experiments and data analysis. T.T.D. provided crystallographic information files. M.K. and S.W.B. wrote the original draft and all authors reviewed and edited the manuscript.

Data Availability Statement

The data that support the findings of this study are available from the corresponding author upon reasonable request.

Reference

[1] S. A. Lee, J. Kim, K. C. Kwon, S. H. Park, H. W. Jang, *Carbon Neutraliz.* **2022**, 1, 26.
[2] D. Li, A. R. Motz, C. Bae, C. Fujimoto, G. Yang, F. Y. Zhang, K. E. Ayers, Y. S. Kim, *Energy and Environ. Sci.* **2021**, 14, 3393.
[3] G. A. Lindquist, S. Z. Oener, R. Krivina, A. R. Motz, A. Keane, C. Capuano, K. E. Ayers, S. W. Boettcher, *ACS Appl. Mater. Interfaces* **2021**, 13, 51917.
[4] R. A. Krivina, G. A. Lindquist, S. R. Beaudoin, T. N. Stovall, W. L. Thompson, L. P. Twight, D. Marsh, J. Grzyb, K. Fabrizio, J. E. Hutchison, S. W. Boettcher, *Adv. Mater.* **2022**, 34, 2203033.
[5] G. A. Lindquist, J. C. Gaitor, W. L. Thompson, V. Brogden, K. J. T. Noonan, S. W. Boettcher, *Energy Environ. Sci.* **2023**, 4373.
[6] M. Maximilian, F. E. Matthias, K. Matthias, A. Frank, B. Maximilian, B. Jan, E. Christian, G. Christian, M. Antonina, A. G. Hubert, *J. Electrochem. Soc.* **2022**, 169, 064505.
[7] C. Mark, M. Z. Christopher, R. Margery, *Catal. Today* **2023**, 420, 114140.
[8] M. Carmo, D. L. Fritz, J. Mergel, D. Stolten, *Int. J. Hydrogen Energy* **2013**, 38, 4901.
[9] F. Scarpelli, N. Godbert, A. Crispini, I. Aiello, *Inorganics* **2022**, 10, 115.
[10] M. Christine, S. Michel, B. Boris, H.-R. Richard, *Int. J. Hydrogen Energy* **2021**, 46, 23581.

[11] Y. Juchan, J. Myeong Je, Z. Xiaojun, P. Yoo Sei, L. Jooyoung, C. Sung Mook, Y. Yadong, *Electrochem. Commun.* **2021**, 131, 107118.
[12] M. J. Jang, J. Yang, J. Lee, Y. S. Park, J. Jeong, S. M. Park, J.-Y. Jeong, Y. Yin, M.-H. Seo, S. M. Choi, K. H. Lee, *J. Mater. Chem. A* **2020**, 8, 4290.
[13] L. Trotochaud, J. K. Ranney, K. N. Williams, S. W. Boettcher, *J. Am. Chem. Soc.* **2012**, 134, 17253.
[14] E. K. Volk, M. E. Kreider, S. Kwon, S. M. Alia, *EES Catal.* **2024**, 2, 109.
[15] P. Janghoon, K. Zhenye, B. Guido, U. Michael, A. M. Scott, *J. Power Sources* **2020**, 479, 228819.
[16] H. Yang, M. Driess, P. W. Menezes, *Adv. Energy Mater.* **2021**, 11, 2102074.
[17] H. Sun, Z. Yan, F. Liu, W. Xu, F. Cheng, J. Chen, *Adv. Mater.* **2020**, 32, 1806326.
[18] O. Romiluyi, N. Danilovic, A. T. Bell, A. Z. Weber, *Electrochem. Sci. Adv.* **2023**, 3, e2100186.
[19] R. A. Krivina, G. A. Lindquist, M. C. Yang, A. K. Cook, C. H. Hendon, A. R. Motz, C. Capuano, K. E. Ayers, J. E. Hutchison, S. W. Boettcher, *ACS Appl. Mater. Interfaces* **2022**, 14, 18261.
[20] P. Wang, B. Wang, *ACS Appl. Mater. Interfaces* **2021**, 13, 59593.
[21] X. Qiucheng, Z. Liyue, Z. Jiahao, W. Jingyu, H. Yanjie, J. Hao, L. Chunzhong, *EnergyChem* **2022**, 4, 100087.
[22] W. Lei, X. Ziang, W. Peican, L. Peng-Fei, X. Qin, W. Baoguo, *Chem. Eng. J.* **2022**, 431, 133942.
[23] Y. Zheng, A. Serban, H. Zhang, N. Chen, F. Song, X. Hu, *ACS Energy Lett.* **2023**, 5018.
[24] T.-H. Kong, P. Thangavel, S. Shin, S. Kwon, H. Choi, H. Lee, N. Park, J.-J. Woo, Y. Kwon, *ACS Energy Lett.* **2023**, 8, 4666.
[25] G. A. Lindquist, S. W. Boettcher *Electrochem. Soc. Interface* **2023**, 32, 32.
[26] L. Zhang, Q. Xu, Y. Hu, L. Chen, H. Jiang, *ACS Sustainable Chemistry & Engineering* **2023**, 11, 13251.
[27] M. Kwak, K. Ojha, M. Shen, S. W. Boettcher, *ACS Energy Lett.* **2024**, 9, 1025.
[28] C. Rong, W. Hsin-Yi, M. Jianwei, Y. Hongbin, L. Bin, *Nano Energy* **2015**, 11, 333.
[29] H. Ji, Y. Ma, Z. Cai, M. Yun, J. Han, Z. Tong, M. Wang, J. Suhr, L. Xiao, S. Jia, X. Chen, *Nanomaterials* **2023**, 13, 749.
[30] Q. Yang, Z. Lu, X. Sun, J. Liu, *Sci. Rep.* **2013**, 3, 3537.
[31] X. Li, G. M. Kale, *J. Phys.: Conf. Ser.* **2006**, 26, 319.
[32] C. B. Mark, P. P. Brad, P. G. Andrew, W. M. L. Leo, R. G. Andrea, C. S. Roger St, *Appl. Surf. Sci.* **2011**, 257, 2717.
[33] J. Xiao, A. M. Oliveira, L. Wang, Y. Zhao, T. Wang, J. Wang, B. P. Setzler, Y. Yan, *ACS Catal.* **2021**, 11, 264.
[34] Q. Yongzhen, L. Jiangjin, C. S. Dinesh, H. Ying, P. Andrea, T. H. Andrew, V. Z. Iryna, *J. Electrochem. Soc.* **2021**, 168, 054502.
[35] K. V. Emily, K. Stephanie, M. A. Shaun, *J. Electrochem. Soc.* **2023**, 170, 064506.
[36] K. S. Wagh, S. M. Mane, A. M. Teli, J. C. Shin, J. Lee, *Micromachines* **2024**, 15, 1450.
[37] M. S. Burke, S. Zou, L. J. Enman, J. E. Kellon, C. A. Gabor, E. Pledger, S. W. Boettcher, *J. Phys. Chem. Lett.* **2015**, 6, 3737.
[38] Y. Itou, N. Ogihara, S. Kawauchi, *J. Phys. Chem. C* **2020**, 124, 5559.
[39] L. R. Shawn, S. I. Eugene, Q. Odeta, D. Yingge, N. K. Sebastien, *Chem. Geol.* **2022**, 605, 120951.

[40] K. Oqmhula, T. Toma, R. Maezono, K. Hongo, *ACS Omega* **2023**, 8, 6743.
[41] M. E. Kreider, H. Yu, L. Osmieri, M. R. Parimuha, K. S. Reeves, D. H. Marin, R. T. Hannagan, E. K. Volk, T. F. Jaramillo, J. L. Young, P. Zelenay, S. M. Alia, *ACS Catal.* **2024**, 14, 10806.
[42] J. Yang, H. Liu, W. N. Martens, R. L. Frost, *J. Phys. Chem. C* **2010**, 114, 111.
[43] V. Pralong, A. Delahaye-Vidal, B. Beaudoin, B. Gérand, J. M. Tarascon, *J. Mater. Chem.* **1999**, 9, 955.
[44] E. Padgett, G. Bender, A. Haug, K. Lewinski, F. Sun, H. Yu, D. A. Cullen, A. J. Steinbach, S. M. Alia, *J. Electrochem. Soc.* **2023**, 170, 084512.
[45] L. Chen, Q. Xu, S. Z. Oener, K. Fabrizio, S. W. Boettcher, *Nat. Commun.* **2022**, 13, 3846.
[46] P. Bhojane, A. Le Bail, P. M. Shirage, *Acta Crystallogr. Sect. C* **2019**, 75, 61.
[47] K. Momma, F. Izumi, *J. Appl. Crystallogr.* **2011**, 44, 1272.
[48] J. Lim, J. M. Klein, S. G. Lee, E. J. Park, S. Y. Kang, S. Maurya, W. E. Mustain, S. Boettcher, Y. S. Kim, *ACS Energy Lett.* **2024**, 9, 3074.
[49] S. Ardizzone, G. Spinolo, S. Trasatti, *Electrochim. Acta* **1995**, 40, 2683.
[50] R. G. Pearson, *Inorg. Chem.* **1988**, 27, 734.
[51] A. Birkel, N. Loges, E. Mugnaioli, R. Branscheid, D. Koll, S. Frank, M. Panthfer, W. Tremel, *Langmuir* **2010**, 26, 3590.
[52] T. Zhai, H. Wang, S. R. Beaudoin, R. Zhang, M. Kwak, S. Hou, Z. Guo, S. W. Boettcher, *J. Am. Chem. Soc.* **2025**, 147, 15448.

TOC

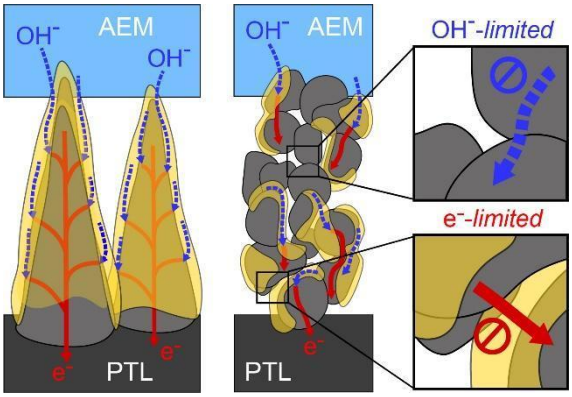

The self-supported Co-based anodes were developed as opposed to nanoparticle ink-based anodes, highlighting the importance of continuous electron and ion transport pathways.